Acta Pharmaceutica Sinica B 2022;12(6):2731–2739

Chinese Pharmaceutical Association
Institute of Materia Medica, Chinese Academy of Medical Sciences

Acta Pharmaceutica Sinica B

www.elsevier.com/locate/apsb
www.sciencedirect.com

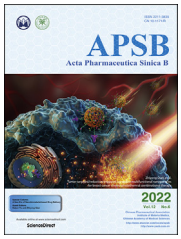

ORIGINAL ARTICLE

Liposome-based multifunctional nanoplatform as effective therapeutics for the treatment of retinoblastoma

Ying Liu[a,b,†], Yu Han[c,†], Shizhu Chen[d], Jingjie Liu[b], Dajiang Wang[b,*], Yifei Huang[b,*]

[a]*Department of Ophthalmology, Beijing Rehabilitation Hospital, Capital Medical University, Beijing 100144, China*
[b]*Department of Ophthalmology, Chinese PLA General Hospital, Beijing 100853, China*
[c]*College of Chemistry & Environmental Science, Chemical Biology Key Laboratory of Hebei Province, Key Laboratory of Medicinal Chemistry and Molecular Diagnosis of the Ministry of Education, Hebei University, Baoding 071002, China*
[d]*China Resources Pharmaceutical Group Limited, Beijing 100000, China*

Received 30 August 2021; received in revised form 6 October 2021; accepted 8 October 2021

KEY WORDS

Nanoplatform;
Liposomes;
Retinoblastoma;
Imaging-guided;
Photothermal therapy

Abstract Photothermal therapy has the characteristics of minimal invasiveness, controllability, high efficiency, and strong specificity, which can effectively make up for the toxic side effects and tumor resistance caused by traditional drug treatment. However, due to the limited tissue penetration of infrared light, it is difficult to promote and apply in clinical practice. The eye is the only transparent tissue in human, and infrared light can easily penetrate the eye tissue, so it is expected that photothermal therapy can be used to treat fundus diseases. Here in, a new nano-platform assembled by liposome and indocyanine green (ICG) was used to treat retinoblastoma. ICG was assembled in liposomes to overcome some problems of ICG itself. For example, ICG is easily quenched, self-aggregating and instability. Moreover, liposomes can prevent free ICG from being cleared through the systemic circulation. The construction of the nano-platform not only ensured the stability of ICG *in vivo*, but also realized imaging-guide

Abbreviations: ARVO, Association for Research in Vision and Ophthalmology; DLS, dynamic light scattering; DPPC, 1,2-dipalmitoyl-*sn*-glycero-3-phosphocholine; DSPE-PEG2000, 1,2-distearoyl-*sn*-glycero-3-phosphoethanolamine-*N*-[(polyethylene glycol)-2000]; EE, encapsulation efficiency; FL, fluorescence; H&E, hematoxylin–eosin; ICG, indocyanine green; ILP, ICG-loaded liposomes; LP, Liposomes; PA, photoacoustic; PBS, phosphate-buffered saline; PDT, photodynamic therapy; PDTX, patient-derived tumor xenograft; PTT, photothermal therapy; Rb, retinoblastoma; TEM, transmission electron microscopy.

*Corresponding authors. Tel.: +86 10 18600574957; fax: +86 10 57975103.
E-mail addresses: glaucomawang@163.com (Dajiang Wang), yfhuang301@163.com (Yifei Huang).
†These authors made equal contributions to this work.
Peer review under responsibility of Chinese Pharmaceutical Association and Institute of Materia Medica, Chinese Academy of Medical Sciences

https://doi.org/10.1016/j.apsb.2021.10.009

photothermal therapy, which created a new strategy for the treatment of retinoblastoma.

1. Introduction

Retinoblastoma (Rb) is the most common primary intraocular malignant tumor in early childhood, which accounts for 6% of all pediatric tumors at the age of 5[1−4]. With the dramatic evolution of diagnosis and management, the prognosis of this devastating and life-threatening malignancy has significantly improved from almost 100% mortality a century ago to over 95% survival rate now[5]. Till now, targeted chemotherapy, especially intra-arterial or intravitreal chemotherapy has been gradually accepted as the first line therapeutic modality complemented by radiotherapy or focal therapy[6−8]. Although targeted chemotherapy is effective to prohibit tumor growth and preserve eyeball, serious post-operative complications, such as systemic symptoms, retinal detachment and vascular events often occur due to drug-induced toxicity or the procedure itself[9−11]. Thus, developing a novel therapeutic strategy is essential for Rb therapy.

Currently, photothermal therapy (PTT) has become an attractive treatment for cancer therapy. Accumulative NIR agents in tumor tissue can prominently increase local temperature by absorbing light energy under NIR laser beams exposure, which effectively and selectively ablate tumor tissue in a minimally invasive method[12,13]. However, most of the existing PTT always focuses on the treatment of solid tumors and is limited by the low penetration depth of infrared light into the tissue, which is difficult to be applied in clinical treatment. Laser therapy is a relatively mature technology in the field of ophthalmic disease treatment, especially for the treatment of fundus diseases. Due to the permeability of the eye tissue, light can easily penetrate the tissue to reach deeper areas. Therefore, the use of PTT to treat fundus diseases has great application prospects.

Till now, various NIR agents, including indocyanine green (ICG)[14−16], gold nanoparticles[17−19], carbon nanodot[20], or graphene oxide[21−23] have been widely employed for evaluating cardiovascular and hepatic function and ophthalmic circulation. ICG is the only NIR agent approved by the FDA[24,25] and can effectively absorb NIR laser and convert it into heat or produce singlet oxygen for PTT and photodynamic therapy (PDT)[26,27]. Furthermore, ICG can also be used for detecting real-time fluorescence (FL) and photoacoustic (PA) imaging of tumor tissue[28], which can provide precise and personalized interventions for cancer therapy. Nevertheless, ICG is instable in aqueous solution by self-quenching and self-aggregation, rapid to be cleared in circulation and lack of targeting[29]. To conquer these drawbacks, various nanocomplexes containing ICG were synthesized to improve ICG stability and enhance tumor accumulation of ICG by passive or active targeting[30−32].

Due to the unique physical and chemical properties of nanomedicine and the brighter application prospects, researchers have developed a variety of nanomedicine delivery systems[33,34]. The most commonly used classification is to classify nanomedicine according to the properties of materials, that is, to classify nanomedicine into inorganic nanomaterials, organic nanomaterials and organic-inorganic hybrid nanomedicine. The biggest feature of nano-medicine based on inorganic materials is its high stability and mature preparation method[35]. Generally, the inorganic nanomaterials developed are all hard materials, and their excellent stability has precisely become the biggest shortcoming that limits their clinical applications. Inorganic materials are difficult to be degraded in organisms, and if they accumulate, their long-term safety will be a major difficulty for drug developers[36]. In contrast, nanomedicine based on organic materials has good biocompatibility, biodegradability and other characteristics, which shows great strength in the application and promotion of nanomedicine. Among them, the most representative organic nanodrugs are liposome and micellar drug delivery system. Most of the nano-drugs currently on the market are liposomal drugs, and many micellar drugs are in clinical trials[37,38].

In the present study, we envisage building a nano-drug carrier system based on liposome loaded with ICG for photothermal treatment to treat fundus Rb. Firstly, a multi-functional ICG-loaded liposomes (ILP) were synthesized for imaging-guided PTT of Rb by encapsulating ICG into lipid bilayer. In addition, the patient-derived tumor xenograft (PDTX) mouse model was established for preclinical research of Rb. The purpose of this study was to confirm that ILP could effectively exert precise and local Rb ablation by PTT, which may be an alternative for chemotherapy, and serve as an outstanding contrast agent for Rb detection.

2. Materials and methods

2.1. Materials

1,2-Dipalmitoyl-*sn*-glycero-3-phosphocholine (DPPC) (P4329), 1,2-distearoyl-*sn*-glycero-3-phosphoethanolamine-*N*-[(poly-ethylene glycol)-2000] (DSPE-PEG_{2000}) (880133P), and indocyanine green (1340009) were from Sigma−Aldrich (St. Louis, MO, USA). Cholesterol (A11470) were from Alfa Aesar (Shanghai, China). Cell Counting Kit-8 (CK04) were purchased from Dojindo (Tokyo, Japan).

2.2. Preparation of ILP and LP

In brief, DPPC, cholesterol and DSPE-PEG_{2000} were mixed in chloroform at a molecular ratio of 55:40:5. Then a thin lipid film was formed by rotary evaporation, after that, the lipid film was dried under vacuum condition for 4 h and hydrated by phosphate-buffered saline (PBS) that contained 1 mg/mL ICG at 65 °C. The final concentration of lipid was 10 mg/mL. Finally, the dispersion was freeze-thawed three times and extruded by 220 nm pore polycarbonate filter. The preparation of LP is the same with ILP but without the ICG addition.

2.3. Characterization of ILP and LP

The morphology and size of ILP and IL were observed by transmission electron microscopy (TEM, HT-7700, Hitachi, Japan). The hydrodynamic diameter and zeta potential were analyzed by laser particle size analyzer (DLS, ZS90, Malvern, UK).

2.4. The encapsulation efficiency of ICG in ILP

After extrusion, the ILP was obtained from aqueous medium by centrifugation at 25,000 r/min for 30 min. Then, free ICG was removed from supernatant and detected by UV/Vis spectrometer at λ_{max} of 740 nm (PerkinElmer, MA, USA). Besides that, the total ICG amount were detected by UV/vis after demulsification by DMSO. The encapsulation efficiency (EE) of ICG was calculated based on Eq. (1):

$$\mathrm{EE}\ (\%) = \left(\mathrm{ICG_{total}} - \mathrm{ICG_{free}}\right)/\mathrm{ICG_{total}} \times 100 \quad (1)$$

2.5. Temperature assessment after NIR irradiation

1 mL PBS containing ICG or ILP (concentration of ICG: 20 μg/mL) was added into 1.5 mL tube. Then, the aqueous media were irradiated with NIR laser (808 nm) at a power intensity of 1.5 W/cm^2 for 10 min and the changes of temperature were measured with an infrared thermal imaging camera (Magnity Electronics Co., Ltd., China).

2.6. Cell culture

Human Rb cell lines Y79 (HTB-18) and WERI-Rb-1 (HTB-169) from the American Type Culture Collection (ATCC, Manassas, USA) were cultured in RPMI 1640 containing 10% fetal bovine serum (FBS) and 1% penicillin/streptomycin at 37 °C in 5% CO_2 (*v*/*v*) atmosphere.

2.7. Cellular uptake

The cellular uptake of ICG and ILP were evaluated using Y79 cells and WERI-Rb-1 cells. First, the cellular uptake of free ICG and ILP were compared. Y79 cells and WERI-Rb-1 cells were incubated with 2 mL culture medium containing free ICG and ILP (concentration of ICG: 10 μg/mL) in 12-well plate (4×10^5 cells per well) for 4 h. Similarly, the cellular uptake of ILP at different time intervals was compared. Y79 cells and WERI-Rb-1 cells were incubated with 2 mL culture medium containing ILP in 12-well plate for various time intervals (1, 2, 3, 4 and 6 h). Then, cells in each well were centrifugated (1500 r/min, 5 min) and washed with PBS trice cells and harvested for quantitative determination of fluorescence intensity by flow cytometry (CytoFLEX S, Beckman, USA) by the PC7 channel (780/60 BP).

2.8. Animals and establishment of PDTX models

Animal experiments were performed in accordance with the Association for Research in Vision and Ophthalmology (ARVO) Statement on the Use of Animals and the Guideline of the Animal Experimental Committee of People's Liberation Army General Hospital (PLAGH) (Beijing, China).

48 SPF-grade male NCG mice (6−8 weeks, weight 18−22 g) were obtained from Nanjing University Model Animal Institute. All mice were housed in an SPF-grade animal facility under a controlled lighting condition (12 h light/12 h dark) and were given free diet.

The PDTX model was established according to the literature[33]. In brief, fresh tumor tissues were obtained from five Rb patients who have not received anti-tumor therapies yet by enucleation in the Department of Ophthalmology of PLAGH. Then, tumor tissues were cut into small pieces of $1.5 \times 1.5 \times 1.5$ mm^3 and immediately put into RPMI 1640 under sterile condition. Tumor samples were subcutaneously injected into mice through a trocar. Once the tumor formed, the length (the longest diameter) and width (the shortest diameter) of tumor were monitored at least twice a week, and tumor volume was calculated based on Eq. (2):

$$\mathrm{Volume\ (T)} = 1/2 \times \mathrm{Length} \times \mathrm{Width}^2 \quad (2)$$

When tumor volume was about 800 mm^2, tumor samples (P1 generation) were excised for serial transplantation (P2 passage).

2.9. In vivo imaging and biodistribution of ILP

When the volume of passaged tumors (P2) was approximately 100 mm^2, mice were randomly divided into two groups ($n = 3$ in each group) and intravenously injected with free ICG and ILP (concentration of ICG: 0.5 mg/kg), respectively. The *ex/in vivo* imaging system (PerkinElmer; excitation) with an excitation filter (704 nm) and emission filter (740 nm) was used for analyzing fluorescence signals of ICG at 0, 4, 8, 12, and 24 h after injection. After *in vivo* imaging, mice were sacrificed and major organs (heart, lung, kidney, spleen and liver) were harvested for *ex vivo* detection of fluorescence signals.

For photoacoustic imaging, two groups of tumor-bearing mice ($n = 3$ in each group) were injected with free ICG and ILP (concentration of ICG: 1 mg/kg) through tail vein, respectively. Then, a PLED photoacoustic system (Prexion Corporation, Tokyo, Japan) was used for semi-quantifying photoacoustic signals of ICG at 0, 4, 8, and 24 h after injection.

2.10. In vivo photothermal therapy

When the volume of passaged tumors (P2) was approximately 100 mm^2, NCG mice were randomly divided into six groups ($n = 6$ in each group). The tumor-bearing mice were intravenously injected with PBS, free ICG and ILP samples at an equivalent dose of 2 mg ICG/kg body weight after 24 h, the tumor region was irradiated with NIR laser (808 nm) at a power intensity of 1.5 W/cm^2 for 8 min. The temperature of tumor tissues during irradiation was monitored by an infrared thermal imaging camera. The tumor volume and body weight of each mouse were monitored at least twice a week. The survival rates of mice in each group were also recorded and calculated.

2.11. Histological examination

The mice were sacrificed within 30 days after treatment and tumor samples and major organs (heart, lung, kidney, spleen and liver) were obtained, fixed and embedded in paraffin. Then, 8-μm section was sliced and stained with hematoxylin–eosin (H&E).

2.12. Statistical analysis

Statistical analysis was performed with SPSS software (version16.0, Chicago, IL, USA). All data were represented as

mean ± SD and analyzed by one-way ANOVA. $P < 0.05$ was considered statistically significant.

3. Results and discussion

3.1. Characterization of ILP

The transmission electron microscopy (TEM) image verified the formation of ILP with a spherical shape and homogeneous distribution (Fig. 1A and B). The surface potential and average hydrodynamic diameter of IL and ILP were measured by dynamic light scattering (DLS). The results showed that the zeta potential of IL and ILP were −20.42 and −22.13 mV, the average hydrodynamic diameter of IL and ILP were 120.32 and 125.14 nm, respectively (Fig. 1C, D and E). In addition, the measured ICG encapsulation efficiency was 95.12 ± 0.78% (Fig. 1E). The stability of prepared ILP was investigated by DLS in PBS. The hydrodynamic diameter and zeta potential were maintained over a period of a month (Fig. 1F). The similar peak absorbance of ILP and ICG indicated that the optical properties of ICG had been maintained after being packaged in ILP (Fig. 1G and H). The above data showed that ILP could be used as an excellent targeted drug delivery platform.

Next, the photothermal effects of ILP had been detected *in vitro*. Under continuous laser irradiation by near-infrared laser (808 nm) with a power of 1.5 W/cm^2, the temperature changes of PBS, ICG and ILP are recorded with an infrared thermal imager (Fig. 1I). At first, the temperature of ILP and ICG increased rapidly, and then decreased slowly as the intermolecular quenching of ICG[39]. In the control group, the PBS irradiated by the same laser showed only a slight increase in temperature. In these two ICG configurations, the highest temperatures of ILP and ICG were 57.2 and 51.5 °C, respectively, which were significantly higher than 34.5 °C of PBS (Fig. 1J). The reason that the peak temperature of ILP was higher than free ICG might be due to the improvement of the stability and the increase of ICG monomer in liposomes[29,40].

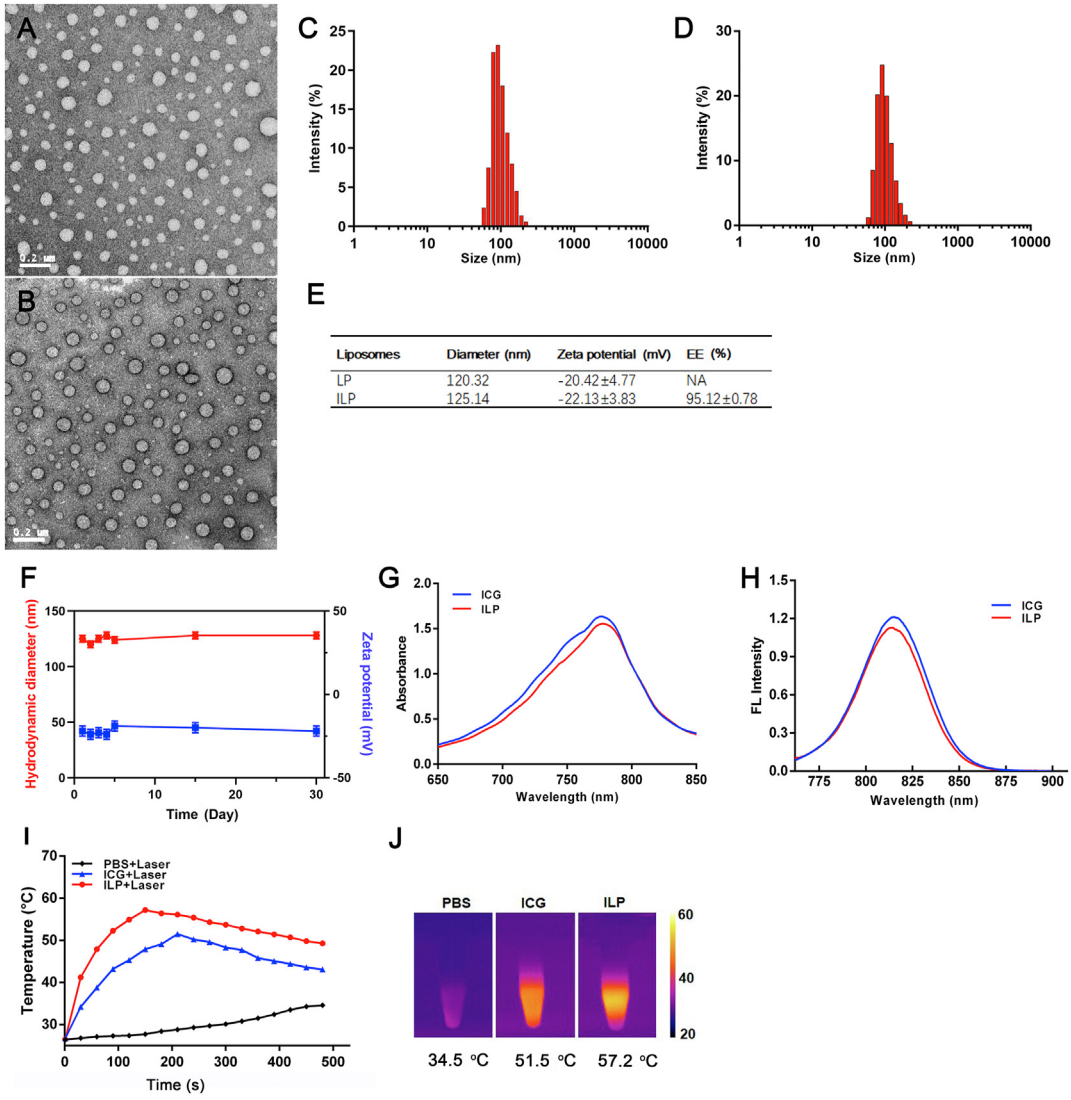

Figure 1 Characterization of ILP. Transmission electron microscope images of LP (A) and ILP (B). Hydrodynamic diameter of LP (C) and ILP (D). (E) Zeta potential and encapsulation efficiency of ILP. (F) The stability of ILP store in PBS over a period of month. (G) UV−vis absorption spectra and (H) the fluorescence spectra free ICG and ILP. (I) The temperature variation and (J) highest-temperature infrared thermal images of PBS, ICG and ILP after exposure under an 808 nm laser (1.5 W).

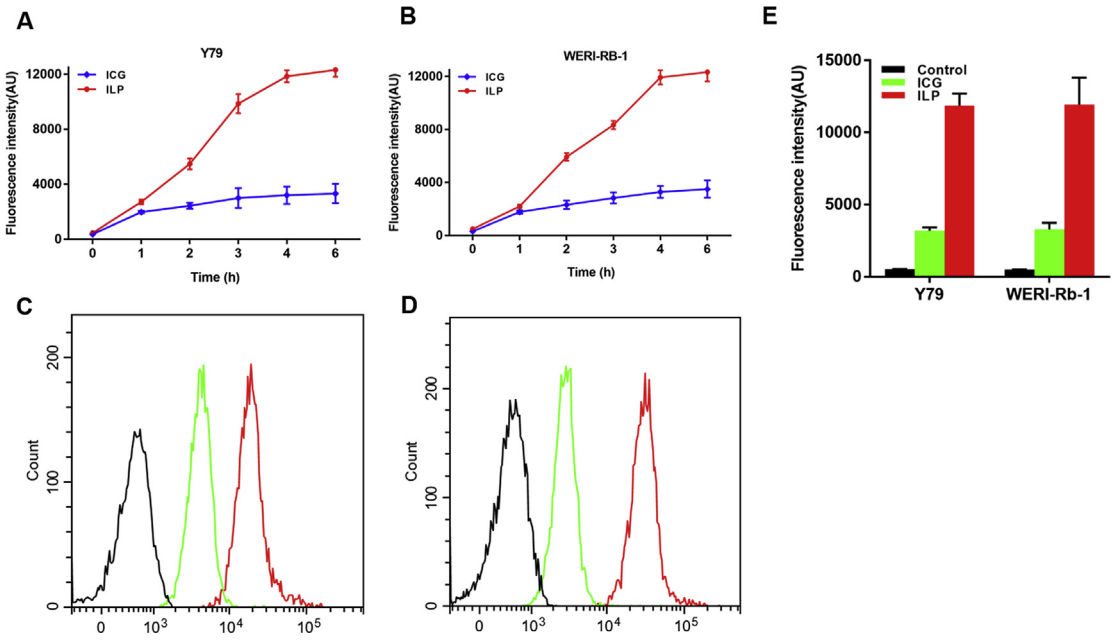

Figure 2 Cellular uptake of ILP and LP. (A) and (B) The statistical graph of the fluorescence intensity (A) for Y79 cells and (B) for WERI-Rb-1 cells. (C) and (D) Flow cytometric analysis of the cellular uptake of free ICG and ILP by Y79 cell (C) and WERI-Rb-1 cell (D) at 4 h. (E) The fluorescence intensity of the cellular uptake of ICG and ILP at 4 h.

3.2. In vitro cellular uptake

Y79 cells and WERI-Rb-1 cells were used to study the uptake behavior of ICG and ILP. The above two cells were incubated with ICG and ILP respectively. And then we collected the cells at 1, 2, 3, 4 and 6 h for flow cytometry analysis. The results showed that the fluorescence intensity of both two cell lines increased with time (Fig. 2A and B). Compared with the cells incubated with free ICG, the fluorescence signal of cells incubated with ILP was significantly enhanced. Quantitatively analysis results showed that the fluorescence intensity of ILP in Y79 cells was about 3.71 times stronger than that of ICG at 4 h (Fig. 2C and E). Likewise, the fluorescence intensity of ILP in WERI-Rb-1 cells was about 3.61 times stronger than that of ICG at 4 h (Fig. 2D and E). It demonstrated that ILP had higher cellular uptake efficiency than free ICG.

3.3. In vivo fluorescence and photoacoustic imaging

In this study, according to the construction method of PDTX model, patient-derived retinoblastoma was transplanted into immunodeficient mice. After continuous observation for several weeks, the tumor cells could maintain the differentiation, morphology, structure and molecular characteristics in mice. The characteristics of blood supply, matrix, growth and necrosis of transplanted tumor in mice were consistent with those of human tumor to a certain extent, which conformed to the biological characteristics of primary tumor. Thereby, these mice could provide a valuable and highly consistent *in vivo* model for the drug treatment of tumor. Therefore, it could be used as a stable and reliable model for tumor treatment in this experiment.

The accumulation behavior and biological distribution of ICG and ILP in Rb mice were observed by FL and PA imaging. After injection of ICG and ILP *in vivo*, high fluorescence signal could be observed in the tumor tissue of mice at initial stage. Then the fluorescence signal attenuated rapidly as ICG and ILP were metabolized from the body. However, the fluorescence intensity of tumor in ILP group was always higher than that in ICG group, which suggested that ILP could be better retained in the blood circulation and accumulated in the tumor (Fig. 3A and B). Due to the limited penetration ability of fluorescence imaging, PA imaging was used for further observation. PA imaging results showed that the strongest PA signal was observed in tumor tissue at 6 h, and then decreased with time (Fig. 3A and C). Similarly, the PA signal of tumor in ILP group was always higher than that in ICG group. Both FL and PA imaging results confirmed the better tumor accumulation ability of ILP.

At the same time, the mice were killed after 6 h of ILP and ICG injection. The fluorescence signal intensity in heart, liver, spleen, lung, kidney and tumor tissue was detected by fluorescence assay. The results showed that ILP had obvious fluorescence accumulation in tumor tissue, while the fluorescence signal intensity of free ICG was weaker. Semi-quantitative analysis of fluorescence intensity in organs *in vitro* showed that in ILP group, the fluorescence ratios of tumor-to-background ($I_{tumor}/I_{background}$), tumor-to-heart (I_{tumor}/I_{heart}), tumor-to-liver (I_{tumor}/I_{liver}), tumor-to-spleen (I_{tumor}/I_{spleen}), tumor-to-lung (I_{tumor}/I_{lung}) and tumor-to-kidney (I_{tumor}/I_{kidney}) were about 3.96, 8.61, 1.63, 2.89, 1.73 and 1.37, respectively. The ratio was significantly higher than that in ICG group (1.83, 3.51, 0.70, 4.16, 1.29, 0.71, Fig. 3D and E). These results confirmed that ICG could been selectively transported to the tumor with high accumulation by ILP[41,42]. Therefore, our results showed that ILP could selectively accumulate in large quantities in tumors, which was very important for the targeted therapy of tumors.

3.4. In vivo photothermal therapy

The photothermal effect of PTT was analyzed by PDTX model. After intravenous injection of PBS, free ICG and ILP, the changes of tumor surface temperature were monitored by infrared thermography at 0, 1, 4 and 8 min. During the whole process, the surface temperature of the three groups increased with time. But that treated by PBS and free ICG only increased to 39.7 and

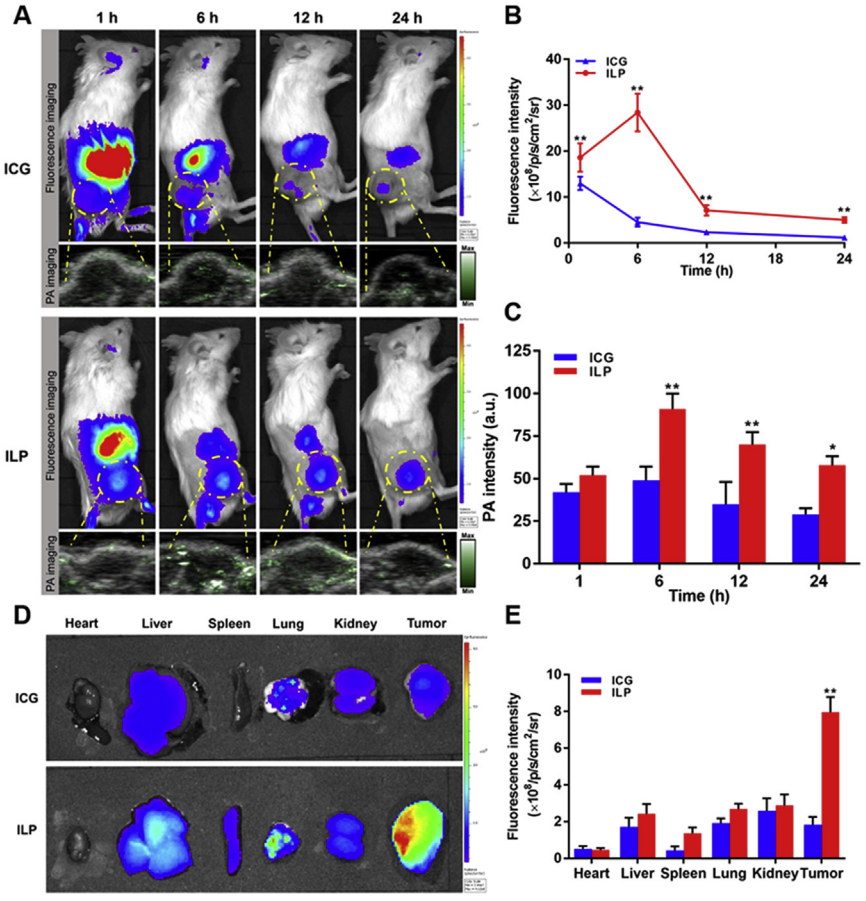

Figure 3 Evaluation of the fluorescence and photoacoustic imaging capacity of ILP. (A) *In vivo* fluorescence and photoacoustic images of ICG and ILP at different time points. (B) and (C) Quantitative analysis of fluorescent intensity (B) and photoacoustic intensity (C) of tumor tissue. (D) *Ex vivo* fluorescence images of ICG and ILP at 6 h. (E) Quantitative analysis of fluorescent intensity of different tissue at 6 h.

43.1 °C (Fig. 4A and B), which was not enough to cause irreversible damage to the tumor[43]. In ILP group, the tumor surface temperature rose rapidly to 53.0 °C in 8 min, which far exceeded the threshold to induce irreversible tissue damage[26]. It was enough to ablate cancer cells.

3.5. *In vivo anti-tumor effect*

In order to further verify the therapeutic effect of ILP, the anti-tumor effect was tested *in vivo*. Six groups were respectively treated by PBS, ICG and ILP, with or without laser irradiation. The changes of tumor volume, body weight and survival rate of mice after treatment in six groups were measured. The tumor volume of PBS + laser, ICG and ILP groups increased significantly with time, and there was no significant difference compared with PBS group (volume was about 900 mm^3), and tumor inhibition rate of all these groups was low. Although the tumor volume of ICG + laser group increased, the trend was slow. And finally the volume reached 500 mm^3, which had a certain delaying effect. The tumor volume of ILP + laser group decreased gradually with the increase of days, and approached zero after 21 days. This showed the ideal anti-tumor effect of ILP which almost completely eliminated the primary tumor in situ (Fig. 4C). In addition, as an indicator of systemic toxicity, the weight of model mice receiving corresponding treatment was evaluated (Fig. 4D). The reduced weight of ILP + laser group may be due the inflammation after the treatment. When the scab was formed at the lesion, the local inflammation was reduced and the animal weight increased. The treated mice did not show severe weight loss, which suggested that neither ICG nor ILP had serious systemic toxicity. Importantly, the survival rate of mice treated by ILP + laser was the highest among all groups (Fig. 4E).

At the same time, the tumors of the mice were dissected and weighed after treatment (Fig. 4F and G). The results showed that there was no significant difference in tumor weight among the PBS group, the PBS + laser group, the ICG group and the ILP group, and there was almost no tumor inhibition effect. However, the tumor weight in ICG + laser group and ILP + laser group was significantly lower than that in control group, which indicated that both of them could delay the growth of tumor to a certain extent. Furthermore, the tumor weight treated by ILP + laser was 83 mg, which was much less than 332 mg in ICG + laser group. This also proved that ILP had the best anti-tumor effect in the above tumor therapy.

Hematoxylin–eosin staining was used to analyze the histology of tumor and organs in mice. Obvious tumor necrosis, severe structural damage and more apoptotic cells could be observed in tumors treated by ILP and laser. In contrast, there were only a few necrotic and apoptotic cells in the tumor tissue accepting other treatments, which further confirmed the phototherapeutic effect of ILP and laser irradiation (Fig. 5B). Histological analysis was also performed in the main organs of mice treated in each group. And no obvious abnormalities were found compared with normal

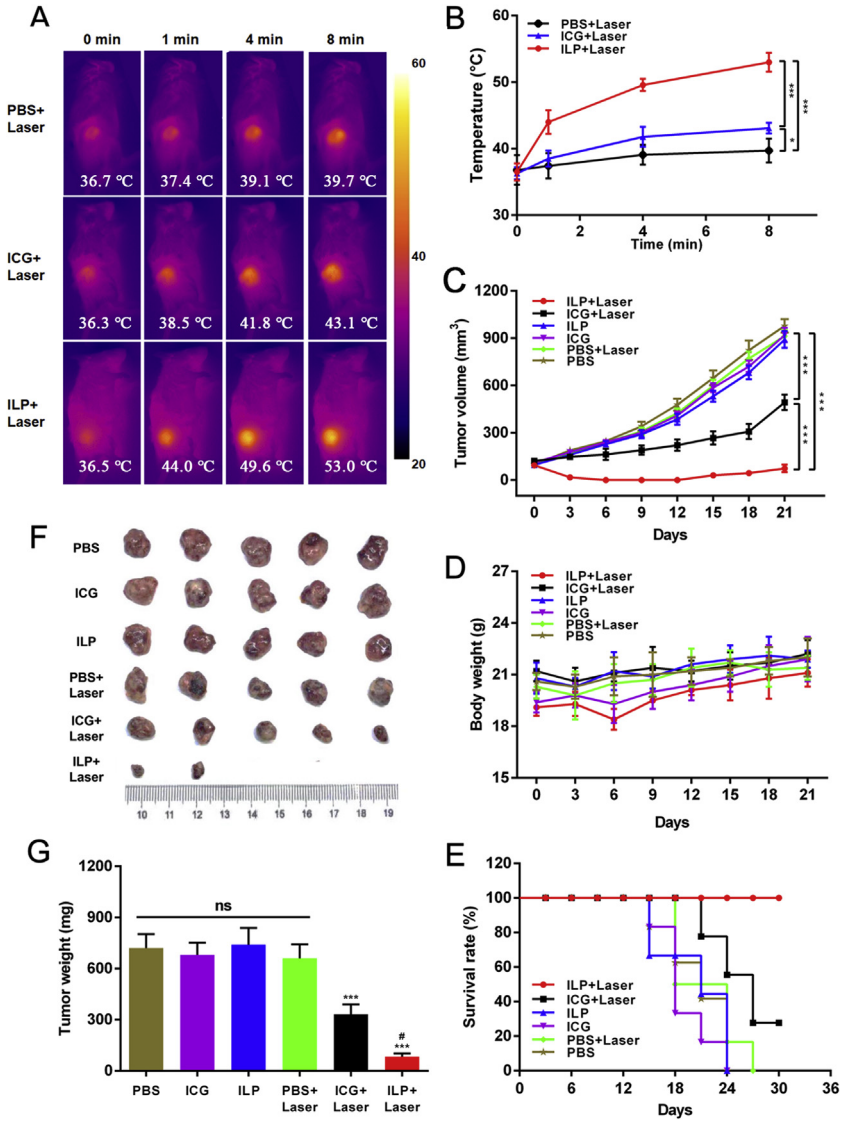

Figure 4 *In vivo* antitumor study. (A) and (B) Photographs (A) and temperature trend (B) of *in vivo* photothermal therapy at different time points. (C)–(E) Tumor volume (C), body weight (D) and survival rate (E) of mice after treatment in all groups. (F) and (G) Photographs (F) and tumor weight (G) of isolated tumor tissue after treatment in all groups.

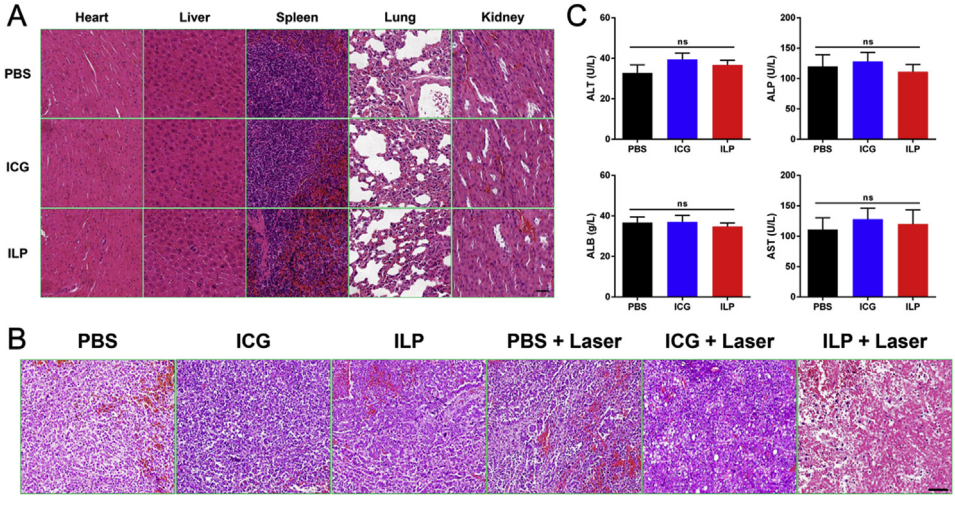

Figure 5 *In vivo* antitumor study. (A) H&E stained images of the heart, liver, spleen, lung, and kidney from the mice in all group. (B) H&E stained images of the tumor from the mice in all groups. (C) Blood biochemical tests of mice after treatment.

mouse organs (Fig. 5A). Obviously, ILP had good tolerance and had no severe acute toxicity to the tested mice.

In fact, how to overcome the damage to normal tissues caused by hyperthermia during treatment is a common problem in the field of photothermal therapy. The development of nanotechnology has made it possible for specific heat transfer. The nanomaterials with NIR light-to-heat conversion are selectively accumulated to the tumor site, and then only the local area of the tumor is illuminated with NIR light. The tumor generates a local ultra-high temperature, which can easily kill the tumor cells. There is very little distribution of nanomaterials in normal tissues around the tumor, and it will not produce excessive temperature under near-infrared irradiation. Therefore, NIR light-mediated heat tumor targeted delivery ensures that normal tissues will not be damaged during treatment, and the safety and effectiveness of hyperthermia are significantly improved.

Furthermore, blood biochemical tests (Fig. 5B) were carried out to determine the potential toxicity of ILP. Compared with the PBS group, the blood biochemical indexes of the ILP and ICG groups were normal and consistent with the reference normal range. This further confirmed that the mice had no adverse reactions to the treatment drugs.

4. Conclusions

In this study, we obtained a new type of nanoparticles named ILP by simulating the natural structure and biological functional properties of the nano-carriers *in vivo*. ILP could achieve specific tumor tissue targeting and penetration *in vitro* and *in vivo*, and had significant advantages in fluorescence imaging and photoacoustic imaging. Moreover, the efficient accumulation of ILP in solid tumors had greatly improved the efficacy of tumor photothermal therapy, which provides a promising strategy for the realization of image-guided tumor phototherapy.

Acknowledgments

This research was financially supported by National Natural Science Foundation of China (7212092, 81770887), China Postdoctoral Science Foundation (2019M650558), Beijing Postdoctoral Research Foundation and Beijing Chaoyang District Postdoctoral Research Foundation.

Author contributions

Ying Liu and Yu Han designed the project. Ying Liu, Yu Han, Shizhu Chen and Jingjie Liu performed the experiments. Yu Han provided experimental drugs and quality control. Ying Liu and Shizhu Chen acquired, analyzed and interpreted the data. Ying Liu and Jingjie Liu drafted the manuscript and Dajiang Wang and Yifei Huang critically revised the manuscript. All of the authors have read and approved the final manuscript.

Conflicts of interest

The authors have no conflicts of interest to declare.

References

1. Pritchard-Jones K, Kaatsch P, Steliarova-Foucher E, Stiller C, Coebergh J. Cancer in children and adolescents in Europe: developments over 20 years and future challenges. *Eur J Cancer* 2006; **42**:2183−90.
2. Broaddus E, Topham A, Singh AD. Incidence of retinoblastoma in the USA: 1975−2004. *Br J Ophthalmol* 2009;**93**:21−3.
3. Fabian ID, Onadim Z, Karaa E, Duncan C, Chowdhury T, Scheimberg I, et al. The management of retinoblastoma. *Oncogene* 2018;**37**:1551−60.
4. Munier FL, Beck-Popovic M, Chantada GL, Cobrinik D, Kivelä TT, Lohmann D, et al. Conservative management of retinoblastoma: challenging orthodoxy without compromising the state of metastatic grace. "Alive, with good vision and no comorbidity". *Prog Retin Eye Res* 2019;**73**:100764.
5. Maccarthy A, Birch JM, Draper GJ, Hungerford JL, Kingston JE, Kroll ME, et al. Retinoblastoma: treatment and survival in great britain 1963 to 2002. *Br J Ophthalmol* 2009;**93**:38−9.
6. Shields CL, Manjandavida FP, Lally SE, Pieretti G, Arepalli SA, Caywood EH, et al. Intra-arterial chemotherapy for retinoblastoma in 70 eyes: outcomes based on the international classification of retinoblastoma. *Ophthalmology* 2014;**121**:1453−60.
7. Dalvin LA, Ancona-Lezama D, Lucio-Alvarez JA, Masoomian B, Jabbour P, Shields CL. Ophthalmic vascular events after primary unilateral intra-arterial chemotherapy for retinoblastoma in early and recent eras. *Ophthalmology* 2018;**125**:1803−11.
8. Francis JH, Iyer S, Gobin YP, Brodie SE, Abramson DH. Retinoblastoma vitreous seed clouds (class 3): a comparison of treatment with ophthalmic artery chemosurgery with or without intravitreous and periocular chemotherapy. *Ophthalmology* 2017;**124**:1548−55.
9. Bianciotto C, Shields CL, Iturralde JC, Sarici A, Jabbour P, Shields JA. Fluorescein angiographic findings after intra-arterial chemotherapy for retinoblastoma. *Ophthalmology* 2012;**119**:843−9.
10. Ravindran K, Dalvin LA, Pulido JS, Brinjikji W. Intra-arterial chemotherapy for retinoblastoma: an updated systematic review and meta-analysis. *J Neurointerventional Surg* 2019;**11**:1266−72.
11. Aronow ME. Intra-arterial chemotherapy for retinoblastoma: experience matters but risks remain. *Ophthalmology* 2018;**125**:1812.
12. Chen Y, Hao Y, Huang Y, Wu W, Liu X, Li Y, et al. An injectable, near-infrared light-responsive click cross-linked azobenzene hydrogel for breast cancer chemotherapy. *J Biomed Nanotechnol* 2019;**15**:1923−36.
13. Xu Y, Hao Y, Li W, Xiao Y, Zhou T, Hu D, et al. Near-infrared responsive doxorubicin loaded hollow mesoporous prussian blue nanoparticles combined with dissolvable hyaluronic acid microneedle system for human oral squamous cell carcinoma therapy. *J Biomed Nanotechnol* 2020;**16**:721−38.
14. Yoon HJ, Lee HS, Lim JY, Park JH. Liposomal indocyanine green for enhanced photothermal therapy. *ACS Appl Mater Interfaces* 2017;**9**:5683−91.
15. Hao Y, Chen Y, He X, Yang F, Han R, Yang C, et al. Near-infrared responsive 5-fluorouracil and indocyanine green loaded MPEG-PCL nanoparticle integrated with dissolvable microneedle for skin cancer therapy. *Bioact Mater* 2020;**5**:542−52.
16. Wu H, Wang C, Sun J, Sun L, Wan J, Wang S, et al. Self-assembled and self-monitored sorafenib/indocyanine green nanodrug with synergistic antitumor activity mediated by hyperthermia and reactive oxygen species-induced apoptosis. *ACS Appl Mater Interfaces* 2019;**11**:43996−4006.
17. Yang K, Liu Y, Wang Y, Ren Q, Guo H, Matson JB, et al. Enzyme-induced *in vivo* assembly of gold nanoparticles for imaging-guided synergistic chemo-photothermal therapy of tumor. *Biomaterials* 2019;**223**:119460.
18. Zhang D, Wu T, Qin X, Qiao Q, Shang L, Song Q, et al. Intracellularly generated immunological gold nanoparticles for combinatorial photothermal therapy and immunotherapy against tumor. *Nano Lett* 2019;**19**:6635−46.
19. Zhong D, Zhao J, Li Y, Qiao Y, Wei Q, He J, et al. Laser-triggered aggregated cubic α-Fe_2O_3@Au nanocomposites for magnetic resonance imaging and photothermal/enhanced radiation synergistic therapy. *Biomaterials* 2019;**219**:119369.

20. Lee C, Kwon W, Beack S, Lee D, Park Y, Kim H, et al. Biodegradable nitrogen-doped carbon nanodots for non-invasive photoacoustic imaging and photothermal therapy. *Theranostics* 2016;**6**:2196.
21. Zhang B, Yu Q, Zhang YM, Liu Y. Two-dimensional supramolecular assemblies based on β-cyclodextrin-grafted graphene oxide for mitochondrial dysfunction and photothermal therapy. *Chem Commun* 2019;**55**:12200−3.
22. Darabdhara G, Das MR, Singh SP, Rengan AK, Szunerits S, Boukherroub R. Ag and Au nanoparticles/reduced graphene oxide composite materials: synthesis and application in diagnostics and therapeutics. *Adv Colloid Interface Sci* 2019;**271**:101991.
23. Hsueh YH, Hsieh CT, Chiu ST, Tsai PH, Liu CY, Ke WJ. Antibacterial property of composites of reduced graphene oxide with nano-silver and zinc oxide nanoparticles synthesized using a microwave-assisted approach. *Int J Mol Sci* 2019;**20**:5394.
24. Bo Q, Yan Q, Shen M, Song M, Sun M, Yu Y, et al. Appearance of polypoidal lesions in patients with polypoidal choroidal vasculopathy using swept-source optical coherence tomographic angiography. *JAMA Ophthalmol* 2019;**137**:642−50.
25. Itakura S, Masui K, Kazama T. Rapid infusion of hydroxyethyl starch 70/0.5 but not acetate Ringer's solution decreases the plasma concentration of propofol during target-controlled infusion. *Anesthesiology* 2016;**125**:304−12.
26. Yan F, Wu H, Liu H, Deng Z, Liu H, Duan W, et al. Molecular imaging-guided photothermal/photodynamic therapy against tumor by iRGD-modified indocyanine green nanoparticles. *J Control Release* 2016;**224**:217−28.
27. Wang Y, Xie D, Pan J, Xia C, Fan L, Pu Y, et al. A near infrared light-triggered human serum albumin drug delivery system with coordination bonding of indocyanine green and cisplatin for targeting photochemistry therapy against oral squamous cell cancer. *Biomater Sci* 2019;**7**:5270−82.
28. Wang R, Zhang C, Li J, Huang J, Opoku-Damoah Y, Sun B, et al. Laser-triggered polymeric lipoproteins for precision tumor penetrating theranostics. *Biomaterials* 2019;**221**:119413.
29. Ma Y, Tong S, Bao G, Gao C, Dai Z. Indocyanine green loaded SPIO nanoparticles with phospholipid-PEG coating for dual-modal imaging and photothermal therapy. *Biomaterials* 2013;**34**:7706−14.
30. Beziere N, Lozano N, Nunes A, Salichs J, Queiros D, Kostarelos K, et al. Dynamic imaging of PEGylated indocyanine green (ICG) liposomes within the tumor microenvironment using multi-spectral optoacoustic tomography (MSOT). *Biomaterials* 2015;**37**:415−24.
31. Zhao P, Zheng M, Yue C, Luo Z, Gong P, Gao G, et al. Improving drug accumulation and photothermal efficacy in tumor depending on size of ICG loaded lipid-polymer nanoparticles. *Biomaterials* 2014;**35**:6037−46.
32. Huang J, Shu Q, Wang L, Wu H, Wang AY, Mao H. Layer-by-layer assembled milk protein coated magnetic nanoparticle enabled oral drug delivery with high stability in stomach and enzyme-responsive release in small intestine. *Biomaterials* 2015;**39**:105−13.
33. Li W, Xue B, Shi K, Qu Y, Chu B, Qian Z. Magnetic iron oxide nanoparticles/10-hydroxy camptothecin co-loaded nanogel for enhanced photothermal-chemo therapy. *Appl Mater Today* 2019;**14**:84−95.
34. Qu Y, Chu B, Wei X, Lei M, Hu D, Zha R, et al. Redox/pH dual-stimuli responsive camptothecin prodrug nanogels for "on-demand" drug delivery. *J Control Release* 2019;**296**:93−106.
35. Chen S, Hao X, Liang X, Zhang Q, Zhang C, Zhou G, et al. Inorganic nanomaterials as carriers for drug delivery. *J Biomed Nanotechnol* 2016;**12**:1−27.
36. Liao J, Jia Y, Wu Y, Shi K, Yang D, Li P, et al. Physical-, chemical-, and biological-responsive nanomedicine for cancer therapy. *Wiley Interdiscip Rev Nanomed Nanobiotechnol* 2020;**12**:e1581.
37. Yang F, Shi K, Jia YP, Hao Y, Peng JR, Qian Z. Advanced biomaterials for cancer immunotherapy. *Acta Pharmacol Sin* 2020;**41**:911−27.
38. Qu Y, Chu BY, Shi K, Peng J, Qian Z. Recent progress in functional micellar carriers with intrinsic therapeutic activities for anticancer drug delivery. *J Biomed Nanotechnol* 2017;**13**:1598−618.
39. Wu L, Fang S, Shi S, Deng J, Liu B, Cai L. Hybrid polypeptide micelles loading indocyanine green for tumor imaging and photothermal effect study. *Biomacromolecules* 2013;**14**:3027−33.
40. Han YH, Kankala RK, Wang SB, Chen AZ. Leveraging engineering of indocyanine green-encapsulated polymeric nanocomposites for biomedical applications. *Nanomaterials* 2018;**8**:360.
41. Sugahara KN, Teesalu T, Karmali PP, Kotamraju VR, Agemy L, Greenwald DR, et al. Coadministration of a tumor-penetrating peptide enhances the efficacy of cancer drugs. *Science* 2010;**328**:1031−5.
42. Kutova OM, Guryev EL, Sokolova EA, Alzeibak R, Balalaeva IV. Targeted delivery to tumors: multidirectional strategies to improve treatment efficiency. *Cancers* 2019;**11**:68.
43. Li Y, Liu G, Ma J, Lin J, Lin H, Su G, et al. Chemotherapeutic drug-photothermal agent co-self-assembling nanoparticles for near-infrared fluorescence and photoacoustic dual-modal imaging-guided chemo-photothermal synergistic therapy. *J Control Release* 2017;**258**:95−107.